A. SKRZAT[1], M. WÓJCIK[1*]

AN IDENTIFICATION OF THE MATERIAL HARDENING PARAMETERS FOR CYCLIC LOADING – EXPERIMENTAL AND NUMERICAL STUDIES

This paper presents the results of experimental studies and numerical simulations of the ratcheting for the PA6 aluminum. In the initial determination of the material hardening parameters, the samples were subjected to the symmetrical strain-controlled cyclic tension-compression test. The experimental stress-strain curve was compared with the numerical one obtained for non-linear Frederick-Armstrong and Voce models. For better fitting of both curves, the optimization procedure based on the least-square method and the fuzzy logic was applied. After establishing the hardening parameters, numerical simulations of the ratcheting were made. The boundary value problem was solved by means of discrete analysis. The data (force and displacement) obtained in numerical computations were used to control the ratchetting experiment. The results of experiments and numerical calculations were compared. Good convergence proves the reliability of the determination of material hardening data.

Keywords: ratchetting, cyclic plasticity, non-symmetrical stress load, finite element method

1. Introduction

Among cyclic plasticity phenomena like strain memory, Bauschinger effect, recovery and hardening, ratchetting plays an important role especially in the safety assessment of engineering structures. Ratchetting is defined as the time-dependent or time-independent cycle by cycle strain accumulation [1] in a material under the stress-controlled cycling with non-zero mean stress (Fig. 1) in line with Eq. (1).

$$\varepsilon^{acc}_{ij} = \int \dot{\varepsilon}^{pl}_{ij} dt \qquad (1)$$

where ε^{acc}_{ij} is the accumulated strain and $\dot{\varepsilon}^{pl}_{ij}$ is the increment of plastic strain. For the closed hysteresis loop $\varepsilon^{acc}_{ij} = 0$.

Ratchetting as a progressive incremental inelastic deformation is characterized by the translation of the stress-strain non-closure hysteresis loop along the strain axis [2]. In consequence, the mean strain (ε_m) during each loading cycle is different from that in the previous one.

The ratchetting phenomenon occurs in various materials, e.g. in austenitic and ferritic steel, in zirconium and titanium alloys, polymers, epoxy resin and ceramic matrix composites where stresses overestimate the material's yield stress [3].
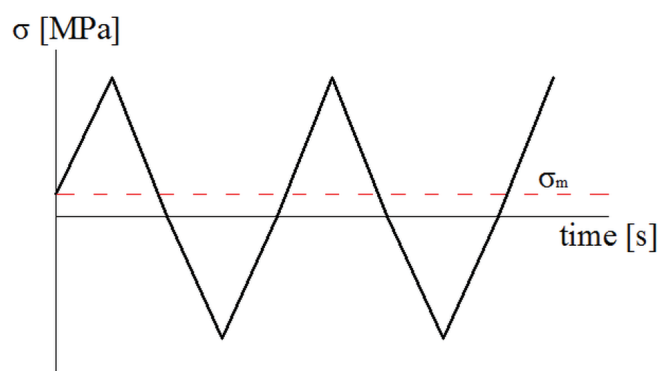

Fig. 1. The stress-time relation for the ratchetting phenomenon

The ratchetting effect depends on the mean stress, the stress rate, the stress level, the loading history as well as the loading path. The mean stress seems to provide a slight influence [4,5]. Considering the value of the mean stress (σ_m), the stabilization after the transient ratchetting is noted for the low mean stress. In contrast, the steady increase of the ratchetting strain is observed for high values of σ_m [6].

Correct prediction of the ratchetting is essential due to the fact that this phenomenon can lead to the catastrophic failure of

1 RZESZOW UNIVERSITY OF TECHNOLOGY, FACULTY OF MECHANICAL ENGINEERING AND AERONAUTICS, DEPARTMENT OF MATERIALS FORMING AND PROCESSING, 8 POWSTAŃCÓW WARSZAWY AVE., 35-959 RZESZÓW, POLAND

* Corresponding author: m.wojcik@prz.edu.pl

structures. The ratchetting phenomenon has been extensively studied in both experimental and numerical studies in recent years. Experiments have been conducted on various materials under different loading conditions. Lim et al. [7] examined the fatigue and the ratchetting of the copper alloy. In [8], the ratcheting phenomenon was investigated for C45 carbon steel. Zhang et al. [9] examined the ratchetting behavior of polyteterafluoroethylene (PTFE) under compressive cyclic loading. The results have shown that the ratchetting is caused by the non-linear visco-elasticity of polymer materials and depends greatly on the mean stress and the stress amplitude. The ratchetting effect in reinforced metal matrix composites subjected to the constant stress and the cyclic change of temperature is described in [10-12]. The experiments of uniaxial and biaxial ratchetting for SA333 Gr. 6 steel at room temperature are presented in [13].The results of uniaxial ratchetting for 316FR steel at room and at high temperature are reported in [14,15]. The ratchetting behavior of epoxy polymer and its effect on the fatigue life is described in [16].

The aim of numerical simulations is a better understanding of the visco-plastic character of materials with the prediction of the ratchetting effect. In [17], the results of numerical simulations of ratchetting behavior for non-saturated granular materials are presented. Gao et al. [18] simulated the ratchetting in pressurized straight low carbon steel pipe under the reversed bending. Chen et al. [19] simulated the multiaxial ratchetting in a medium carbon steel. The results of numerical simulations of the uniaxial ratchetting for solder alloys are contained in [20]. In [21], the results of simulations of a multiaxial ratchetting and a nonproportional cyclic deformation of IN738LC at high temperatures are shown. The finite element analysis of ratchetting behavior of the glass fiber reinforced epoxy composites under cycling loading are also described in [22]. The dependence between the uniaxial ratchetting and the mean stress as well as the stress-strain characteristic was found.

The non-symmetrical cyclic loading tests require a very precise identification of material's hardening parameters. It was shown [23], that the kinematic hardening did not affect the ratchetting progression. However, ratchetting phenomenon is very sensitive to the isotropic hardening. Depending on the isotropic hardening parameters describing the stabilization rate of a material in the cyclic tension-compression test, the gradual deceleration, quasi-shakedown or even the blocking of the ratchetting are noted [23,24].

The uniaxial tension tests are not enough to determine the hardening parameters required for the ratchetting simulations. The cyclic tension-compression test is commonly applied for these parameters identification. In [25], the cyclic tension-compression test is used in the identification of kinematic hardening material parameters for accurate springback predictions. The application of the cyclic tension-compression test for the determination of material parameters is described in [26]. In [27], tension-compression as well as cyclic shear tests are used for the identification of kinematic hardening parameters.

In this paper, the uniaxial ratcheting behavior of PA6 aluminum alloy was studied under the non-symmetrical cyclic tension-compression test. The paper objectives are as follows:
– the identification of material's hardening parameters on the basis of an experimental stress-strain curve obtained by the cyclic tension-compression test,
– the enhancement of hardening parameters with the use the optimization procedure based on the least-square method as well as on the fuzzy logic,
– the numerical simulation of ratchetting including hardening parameters identified earlier,
– the experimental verification of numerical tests and validation of computed hardening data.

A good knowledge of the ratchetting phenomenon might be useful to set up forming operations conditioned by the cyclic loading, including the KOBO extrusion method introduced by Korbel, Bochniak and investigated by other researchers [28-31].

2. Cyclic tension-compression tests

The PA6 aluminum characterized by the high strength is widely used in civil engineering, in automotive industry as well as in boat building [32]. In spite of the widespread use of PA6 aluminum in various industry sectors, the studies on the ratchetting of PA6 material are limited.

The geometry of specimens made of PA6 aluminum used in this research is shown in Fig. 2. The chemical composition of PA6 aluminum is Al-96.73%, Si-0.9%, Fe-0.45%, Cu-0.09%, Mn-0.6%, Mg-0.7%, Cr-0.25%, Zn-0.2% and Ti-0.08%. The mechanical properties of PA6 aluminum are $E = 72\,000$ MPa and $\vartheta = 0.33$.
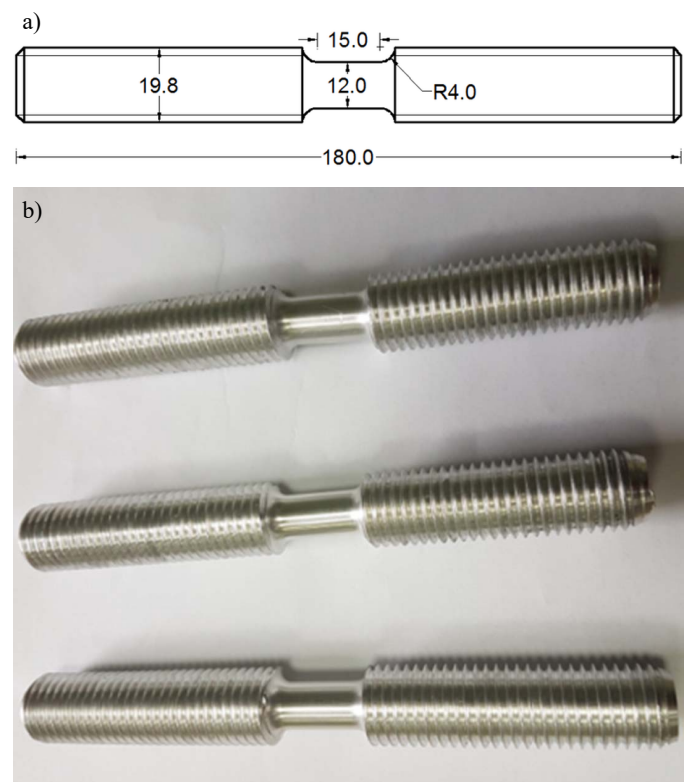

Fig. 2. Specimens geometry (a), real photo (b)

Firstly, the strain-controlled symmetrical cyclic tension-compression test was done for the preliminary determination of the material hardening parameters. The experiment was carried out at room temperature using ZWICK/ROELL Z100 testing machine (Fig. 3). The deformation ±2% of the measuring base was applied. The experiment was carried out in triplicate and the results were averaged.

Fig. 3. ZWICK/ROELL Z100 testing machine (a) and the sample's mount (b)

In this part of the research the experimental stress-strain curve is obtained shown in Fig. 4. Engineering stress σ_{nom} and engineering strain ε registered in this test were transferred into the true once with the application of Eq. (2) and (3).

$$\sigma = \sigma_{nom}(1 + \varepsilon) \qquad (2)$$

$$\varphi = \ln(1 + \varepsilon) \qquad (3)$$

where φ and σ are true strain and stress. Eq. 2 is derived with the assumption that the plastic deformation of the constant volume of the specimen is preserved.
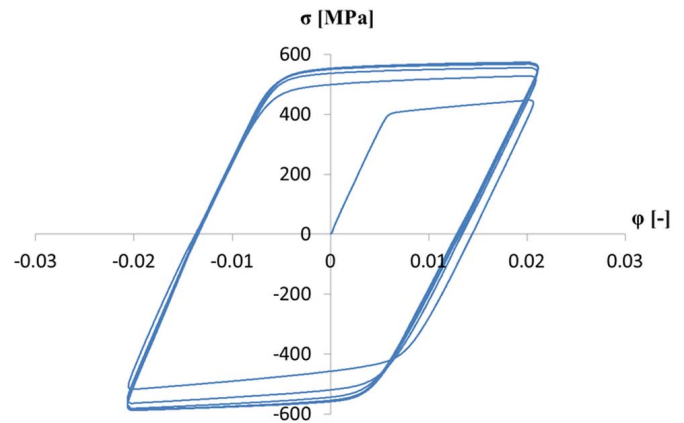
Fig. 4. The experimental true stress-true strain curve for PA6 aluminum

On the basis of the hysteresis loops shown in Fig. 4, the initial selection of the hardening parameters is made. The following parameters are designated [33]:

– the number of loops up to hysteresis stabilization – parameter b,
– the extrapolated translation of the yield stress for the final stable hysteresis loop – the c/γ ratio,
– the slope of the plastic response – parameter γ,
– the size of the initial and the final stable yield surfaces – parameter Q.

The following hardening parameters are selected using the experimental stress-strain curves: Q = 150 MPa, c = 12,200 MPa, γ = 238 and b = 10. The hardening models based on these parameters are described in the next section.

3. Problem formulation for isotropic and kinematic hardening

Many constitutive models have been proposed to describe the elastoplastic behavior of materials under the cycling loading conditions. The first cyclic plasticity model using a multiple surface kinematic hardening rules was proposed by Mróz [34]. The modification of such model was presented by Dafalias, Popov and Krieg [35-38]. Among others, Chaboche, Frederick-Armstrong, Mróz two-surface and Ohno-Wang models are commonly used in numerical simulations of the ratchetting phenomenon [34,39-41]. In this research, Frederick-Armstrong

non-linear kinematic model [42] including the Bauschinger effect was applied (Eq. 4)

$$dx = \frac{2}{3}cd\varepsilon^p - \gamma x dp \qquad (4)$$

or after integration in terms of the magnitude x (Eq. 5).

$$x = \frac{c}{\gamma}\left(1 - e^{-\gamma\varepsilon^p}\right) \qquad (5)$$

Here: x is the backstress, ε^p is the plastic strain, c and γ are materials constants.

The Voce isotropic hardening model is described by Eq. (6) or Eq. (7)

$$dr(p) = b(Q - r)dp \qquad (6)$$

$$r(p) = Q(1 - e^{-bp}) \qquad (7)$$

where b and Q are materials constants, p is the equivalent plastic strain and r is the increase in the yield stress.

The formulation is completed by the following formulas:
– the Hook's law in the incremental form (Eq. 8)

$$d\boldsymbol{\sigma} = \boldsymbol{C}\,d\boldsymbol{\varepsilon} \qquad (8)$$

where $\boldsymbol{C}$ is the constitutive matrix.
– For small strains, strain $\boldsymbol{\varepsilon}$ is additively decomposed into elastic $\boldsymbol{\varepsilon}^e$ and inelastic $\boldsymbol{\varepsilon}^p$ (plastic) parts (Eq. 9)

$$\boldsymbol{\varepsilon} = \boldsymbol{\varepsilon}^e + \boldsymbol{\varepsilon}^p \qquad (9)$$

– In the context of time-independent material behavior, the von Mises yield criterion is described by Eq. (10) [43]

$$f\left(\boldsymbol{\sigma}, \boldsymbol{x}, p\right) = \sqrt{\frac{3}{2}\left(\boldsymbol{\sigma}' - \boldsymbol{x}\right):\left(\boldsymbol{\sigma}' - \boldsymbol{x}\right)} - \sigma_y - r\left(p\right) \qquad (10)$$

where $\boldsymbol{\sigma}$ and $\boldsymbol{\sigma}'$ are the stress and the deviatoric stress, σ_y is the yield stress and p is the equivalent plastic strain.
For the plastic flow (Eq. 11):

$$f(\boldsymbol{\sigma}, \boldsymbol{x}, p) = 0 \qquad (11)$$

– The consistency condition is described by the formula (Eq. 12) [44]

$$df = \frac{\partial f}{\partial \boldsymbol{\sigma}}d\boldsymbol{\sigma} + \frac{\partial f}{\partial \boldsymbol{x}}d\boldsymbol{x} + \frac{\partial f}{\partial p}dp \qquad (12)$$

– The normality condition is (Eq. 13) [33]

$$d\boldsymbol{\varepsilon}^p = d\lambda\frac{\partial f}{\partial \boldsymbol{\sigma}} \qquad (13)$$

where $d\boldsymbol{\varepsilon}^p$ is the increment of plastic strain and $d\lambda$ is the plastic multiplier which can be found from the consistency condition (Eq. 12).
– The plastic flow rule associated with the von Mises yield criterion gives (Eq. 14) [45]

$$d\boldsymbol{\varepsilon}^p = d\lambda\frac{3\boldsymbol{\sigma}'}{2\sigma_e} \qquad (14)$$

where σ_e is the effective stress.

Equations (4)-(14) are used in developing the numerical program, which for the assumed strain increment calculates the stress increment. This way hysteresis loops are numerically generated for the deformation history assumed and for various magnitudes of the strain hardening parameters. In the numerical program explicit integration is executed. Since this type of integration is conditionally stable, 4000 strain increments are made for the single hysteresis loop, while only 400 are necessary to achieve the convergence.

4. Numerical approximation of experimental results

Theoretical formulation and numerical program presented in section 3 are used in generation of strain-stress curves obtained for preliminary selected material hardening parameters (Fig. 5).
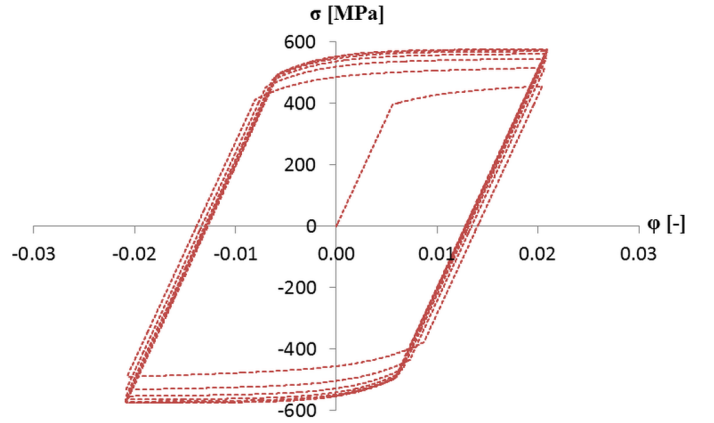

Fig. 5. The numerical true stress-true strain curve for PA6 aluminum

The authorial original methodology was developed for the enhancement of material hardening parameters. The detailed information about the procedure is contained in [33]. Here only an essential description is included. Firstly, the optimization process with the use of the least-square method was done to achieve the better agreement of the experimental and numerical curves. In this approach, all hardening parameters were randomly distorted and for each set of hardening parameters, the error norm was computed in line with Eq. (15)

$$\|B\| = \sqrt{\int_\varepsilon\left(\sigma_{exp} - \sigma_{app}\right)^2 d\varepsilon} \qquad (15)$$

where σ_{exp} and σ_{app} are experimental and approximation stress values, respectively.

The minimum approximation error using the least square method is reached for the following data: $Q = 146.8$ MPa, $c = 11{,}010$ MPa, $\gamma = 274.8$ and $b = 11.3$. The comparison of the experimental and numerical curves for the above parameters is shown in Fig. 6.

It is worth noting that similar small error norm might be obtained for different sets of hardening parameters. Thus the
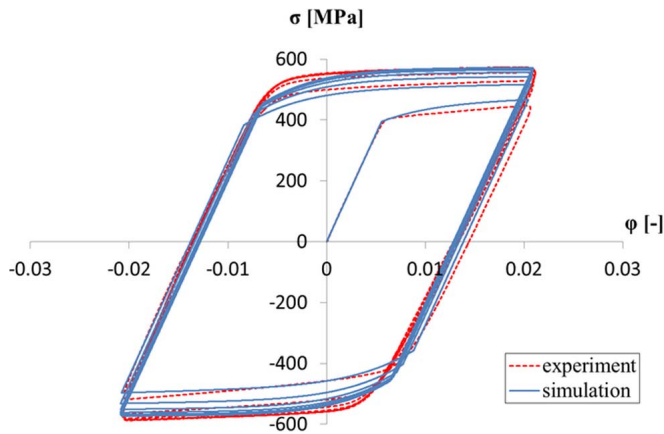
Fig. 6. The experimental curve and numerical curve after the optimization approach

important question arises: which set of the hardening parameters gives the best approximation? In this research the fuzzy logic was applied as the objective tool for optimal selection of the hardening parameters. Such an approach assumes some uncertainty of the hardening data [46-50]. In our approach, the hardening parameters (Q,b,c,γ) were assumed to be fuzzy input variables. The triangular membership functions for the input variables were built in the fuzzification step. The fuzzy analysis was performed and fuzzy output variable (the error norm B) as well as its membership function were obtained.

The α-optimization procedure was used as the main method in the fuzzy analysis. This approach is based on the separation of membership functions for input variables x and y into α-levels for which the values $(x_{\alpha kl}, x_{\alpha kr}, y_{\alpha kl}$ and $y_{\alpha kr})$ are computed (Fig. 7). For randomly selected $x \in [x_{\alpha kl}, x_{\alpha kr}]$ and $y \in [y_{\alpha kl}, y_{\alpha kr}]$, the minimum $z_{\alpha kl}$ and maximum $z_{\alpha kr}$ are found (Eq. 16) [49]. Extreme z values for all α-levels determine the shape of the fuzzy otput membership function $\mu(z)$.

$$\begin{cases} z = f(x,y) \rightarrow \min(x,y) \in X_\alpha \\ z = f(x,y) \rightarrow \max(x,y) \in X_\alpha \end{cases} \quad (16)$$
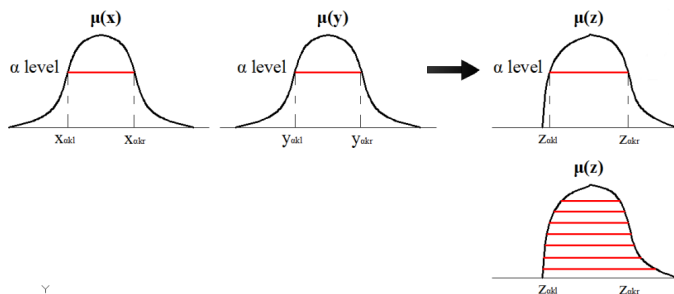

Fig. 7. The schematic representation of α-optimization method

The method limitations are the continuity of the mapping operation and the convexity of the fuzzy results space (Eq. 17).

$$\mu_A(x_2) \geq \min[\mu_A(x_1),$$
$$\mu_A(x_3)] \forall x_1, x_2, x_3 \in X \wedge \frac{n!}{r!(n-r)!} x_1 \leq x_2 \leq x_3 \quad (17)$$

The α-optimization method gives a relatively smooth shape of the output membership function in comparison to other fuzzification methods, e.g. the extension principle. Thus, the α-optimization method was used as the main numerical tool in this research. The extension principle described in [33, 49] was applied only in order to check the convexity and the consistency of the results obtained in the fuzzy analysis.

The most reliable value (z_0) is found in the defuzzification step using the mass center method (Eq. 18) [46].

$$z_0 = \frac{\int z \cdot \mu(z)\,dz}{\int \mu(z)\,dz} \quad (18)$$

where $\mu(z)$ is the membership function of z variable. The set of the fuzzy x and y variables which afford the minimum of z_0 value is assumed to be optimal.

In the above description x and y are any of Q,b,c,γ hardening parameters, while z is the error norm (Eq. 15).

The numerical curve obtained with the use of fuzzy logic is shown in Fig. 8. The hardening parameters indicated with the application of the fuzzy logic approach are: Q = 125.8 MPa, c = 12,181.1 MPa, γ = 215.8 and b = 10.6 (B = 16.3%).

In spite of the use of the model based on only four parameters, a relatively good agreement between numerical and experimental curves was obtained. The better fitting of both curves might be obtained for multiparametric models, e.g. for Chaboche model.
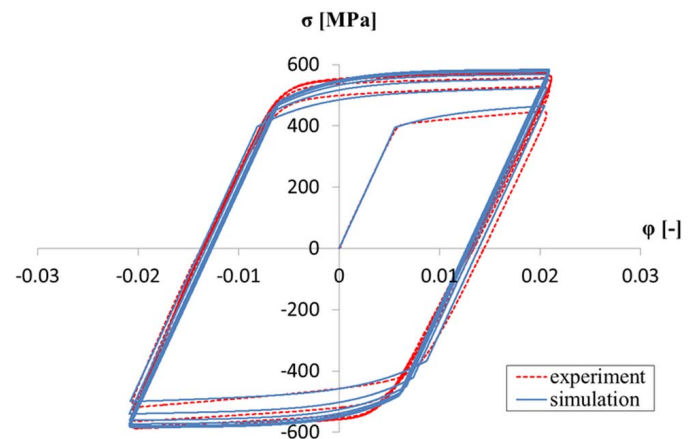

Fig. 8. The numerical curves after the fuzzy logic optimization

5. The non-symmetrical cyclic tension-compression tests

Before experimental investigation of the ratchetting phenomenon numerical simulation of the non-symmetrical stress-controlled cyclic tension-compression test was carried out using finite element method and commercial ABAQUS program. For the assumed load history (stress) shown in Fig. 10, the material response (strain) is computed. The yield should occur for all the tension and compression load cases.

The numerical simulation was carried out for the sample made of PA6 aluminum alloy with 11.97 mm diameter and the

length of 15 mm (Fig. 9). In the FEM analysis the sample was modeled as an axisymmetric deformable body and was discretized by two-dimensional quadratic quadrilateral elements. Appropriate boundary conditions are applied at one of the ends of the sample. The variation of the pressure applied for the other need is shown in Fig. 10.

The following material data are used in this analysis: Young's modulus – $71 \cdot 10^3$ MPa, Poisson's ratio – 0.33, the yield stress – 395 MPa. The hardening parameters identified in the cyclic tension-compression test and optimized by means of fuzzy logic were applied in numerical calculations.
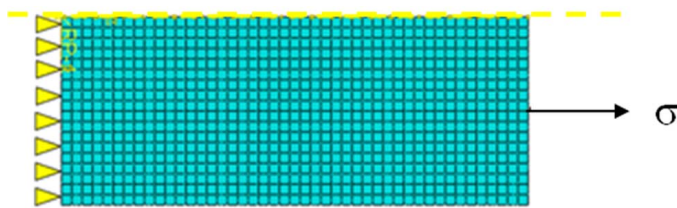

Fig. 9. The model used in a numerical analysis of the non-symmetrical stress-controlled cyclic loading
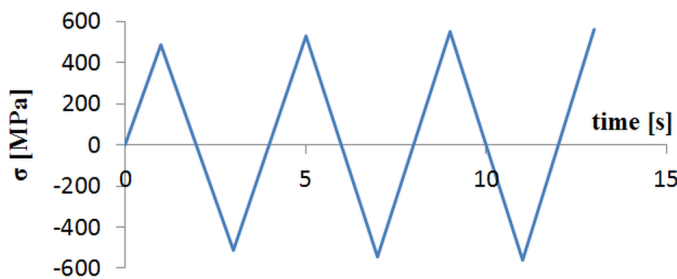

Fig. 10. The amplitude of load applied in numerical simulation

After solving boundary value problem the following results are obtained: the stress-strain curve (Fig. 11), the variation of the normal force (Fig. 12a) and the specimen deformation (Fig. 12b). The last two resultants are the control parameters in experimental investigations made on testing machine. Experimental investigation are made in order to validate proposed numerical model and its hardening parameters.
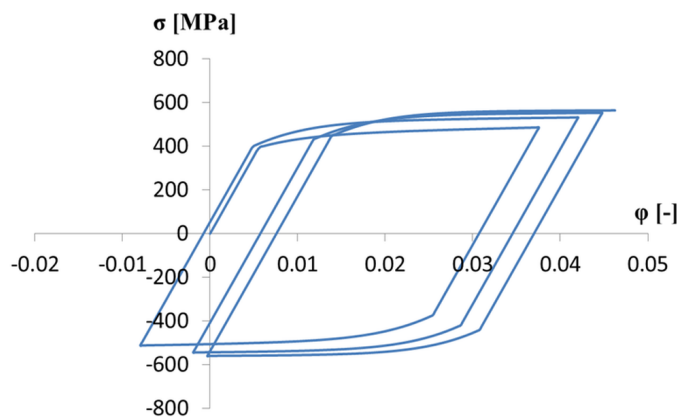

Fig. 11. The numerical stress-strain curve for a non-symmetrical stress-controlled cyclic loading
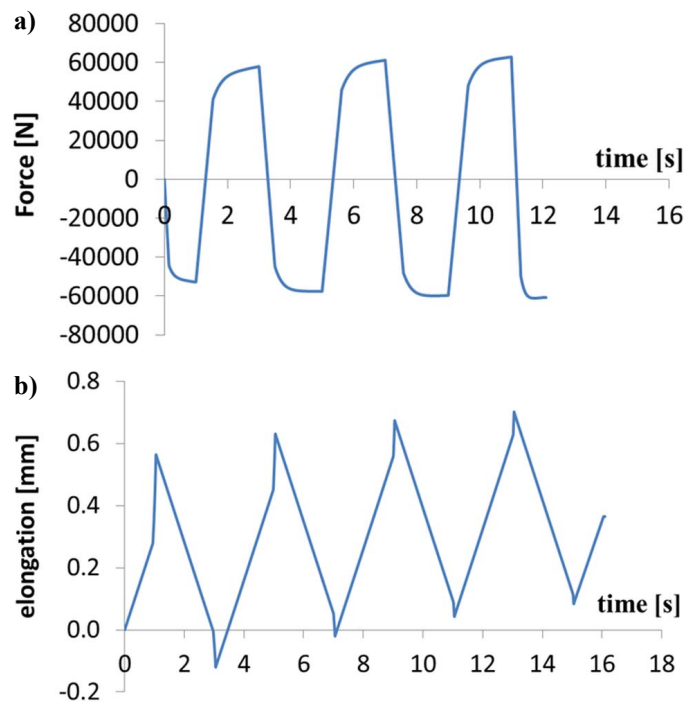

Fig. 12. The force (a) and elongation (b) distribution obtained in numerical simulations

In the next part of presented research, the results of the numerical simulation were compared with experimental data. The non-symmetrical cyclic tension-compression test was carried out for two samples using ZWICK/ROELL Z100 testing machine. In the first test, the displacement variation shown in Fig. 12b is used as the control parameter. The comparison of true stress-true strain curves obtained experimentally and numerically is shown in Fig. 13. It can be clearly seen, that a very good agreement between theory and experiment is achieved which confirms the proper selection of the material hardening data.
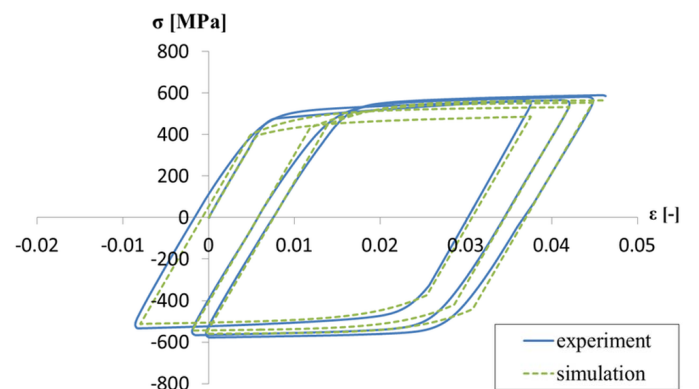

Fig. 13. The true stress-true strain relations registered in experimental and numerical tests

From the scientific point of view the comparison of the theoretical solution and the experimental results for the force-controlled test might be interesting (see Fig. 12a). This is an ill-conditioned problem i.e. small variation of the force (stress) can provide a large variation of the deformation (strain).
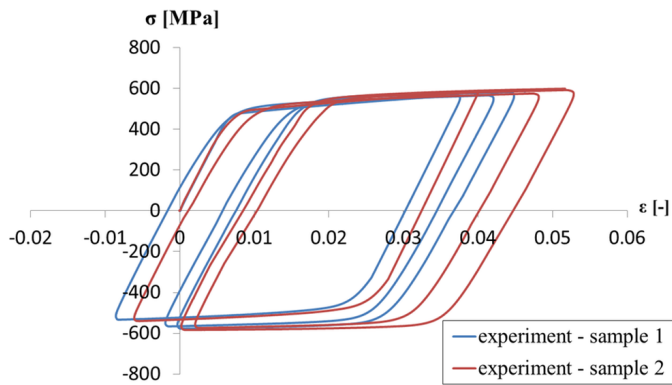
Fig. 14. The hysteresis loop registered for two identical samples (experiment controlled by force)

Unfortunately, such an experiment provides scattered results. In Fig. 14 there are presented the results of the force-controlled experiment made for two identical samples. One may notice that two experiments carried out in exactly the same conditions provide responses qualitatively similar but quantitatively different. For this reason we do not compare the results of numerical simulations with the results of force-controlled experiments.

6. Summary and conclusions

Numerical simulation of the non-symmetrical cyclic tension-compression test for a PA6 aluminum alloy and its experimental verification are presented in this paper. The modeling of the ratchetting phenomenon requires precise determination of the material hardening parameters.

In this research the material hardening parameters are indicated in the symmetrical strain-controlled cyclic tension-compression test. On the basis of the experimental stress-strain curve, the preliminary selection of hardening parameters was done. Numerically generated hysteresis loops for Frederick-Armstrong and Voce models are compared to experimental curves. For better fitting the optimization procedure based on the least-square method and the fuzzy logic approach was applied. In spite of the use of the theoretical model based on only four hardening parameters, the relatively good agreement between numerical and experimental curves was obtained. However, the application of multiparameter models, e.g. the Chaboche model enables to achieve the better compatibility. The general methodology of the identification of hardening parameters presented in this paper will be a very effective tool for identification of the material hardening parameters in more complicated multiparameter models.

The numerical simulation of the non-symmetrical stress-controlled cyclic tension-compression test was done by finite element method analysis. The results of the numerical simulations i.e. the force and displacement distributions were used later on in the experimental research of non-symmetrical cyclic loading. A very good agreement is achieved between numerical simulations and experiment carried out for the ratchetting response. This confirms the proper selection of the material hardening data. But it is worth noting that experiments carried out for two identical samples in exactly the same conditions provide responses qualitatively similar but quantitatively different.

Further research will focus on the determination of material hardening parameters from the non-symmetrical stress-controlled cyclic loading tests. Such test is very sensitive to small variations of the hardening parameters.

REFERENCES

[1] G. Kang, Int. J. Fatigue **30**, 1448-1472 (2008).

[2] M. Noban, H. Jahed, Int. J. Pres. Ves. Pip. **84**, 223-233 (2007).

[3] M. Shariati, H. Hatami, H. Yarahmadi, H.M. Eipakchi, Mater. Design **34**, 302-312 (2011).

[4] Q. Dong, P. Yang, G. Xu, Int. J. Nav. Archit. Ocean Eng. **11**, 671-678 (2019).

[5] S.S. Manson, G.R. Halford, Fatigue and Durability of Structural Materials, ASM International, Ohio (2006).

[6] S.K. Paul, J. Mater. Res. Technol. **8**, 4894-4914 (2019).

[7] C.-B. Lim, K.S. Kim, J.B. Seong, Int. J. Fatigue **31**, 501-507 (2009).

[8] X. Yang, Int J Fatigue **27**, 1124-1132 (2005).

[9] Z. Zhang, X. Chen, T. Wang, Polym. Eng. Sci. **48**, 29-36 (2007).

[10] S. Guo, G. Kang, J. Zhang, Int. J. Plasticity **40**, 101-125 (2013).

[11] S. Guo, G. Kang, J. Zhang, Int. J. Plasticity **27**, 1896-1915 (2011).

[12] G. Kang, S. Guo, C. Dong, Mater. Sci. Eng. A **426**, 66-76 (2006).

[13] S.C. Kulkarni, Y.M. Desai, T. Kant, G.R. Reddy, Y. Parulekar, K.K. Vaze, Int. J. Pres. Ves. Pip. **80**, 179-185 (2003).

[14] N. Ohmo, M. Abdel-Karim, M. Kobayashi, T. Igari, Int. J. Plasticity **14**, 355-372 (1998).

[15] N. Ohno, M. Abdel-Karim, J. Eng. Mater. Technol. **122**, 35-41 (2000).

[16] G. Tao, Z. Xia, Polym. Test. **26**, 451-460 (2007).

[17] F. Alonso-Marroquin, H.J. Herrmann, Phys. Rev. Lett. **92**, 1-4 (2004).

[18] B.J. Gao, X. Chen, G. Chen, Int. J. Pressure Vessels Piping **83**, 96-106 (2006).

[19] X. Chen, R. Jiao, K.S.Kim, Int. J. Plasticity **21**, 161-184 (2005).

[20] K. Sasaki, K-i. Ohguchi, J. Electron. Mater. **40**, 2403-2414 (2011).

[21] M. Abdel-Karim, M. Mizuno, N. Ohno, J. Soc. Mater. Sci. **48**, 104-109 (1999).

[22] X. Chen, S.C. Hui, Polym. Test **24**, 829-833 (2005).

[23] X. Chen, R. Jiao, Int. J. Plast. **20** (4-5), 871-898 (2004).

[24] O.U. Colak, Mater. Design. **29** (8), 1575-1581 (2008).

[25] P.-A. Eggertsen, K. Mattiasson, Int. J. Mater. Form. **42** (2), 103-120 (2011).

[26] T. Phongsai, W. Julsri, B. Chongthairungruang, S. Suranuntchai, S. Jirathearanat, V. Uthaisangsuk, Songklanakarin J. Sci. Technol. **38** (5), 485-493 (2016).

[27] M. Rosenschon, S. Suttner, M. Merklein, Key Eng. Mater. **639**, 385-392 (2015).

[28] W. Bochniak, K. Marszowski, A. Korbel, J. Mater. Process. Technol. **169** (1), 44-53 (2005).

[29] W. Bochniak, A. Korbel, J. Mater. Process. Technol. **134** (1), 120-134 (2003).

[30] W. Bochniak, A. Korbel, P. Ostachowski, S. Ziółkiewicz, Obróbka Plastyczna Metali **24** (2), 83-87 (2013).

[31] K. Pieła, L. Błaz, M. Jaskowski, Arch. Metall. Mater. **58** (3), 683-689 (2013).

[32] D. Bańkowski, S. Spadło, Arch. Foundry Eng. **17**, 19-24 (2017).

[33] M. Wójcik, A. Skrzat, Continuum Mech. Thermodyn. 1-12 (2019), DOI: 10.1007/s00161-019-00805-y.

[34] Y. Jiang, H. Sehitoglu, Int. J. Solids. Struct. **33**, 1053-1068 (1996).

[35] Y.E. Dafalias, E. Popov, Acta Mech. **21**, 173-192 (1975).

[36] G.Z. Voyiadjis, S.M. Sivakumar, Studies in Applied Mechanics **35**, 253-295 (1994).

[37] R.D. Krieg, ASME J. Appl. Mech. **42**, 641–646 (1975).

[38] Y. Dafalias, E. Popov, ASME J. Appl. Mech. **43**, 645-650 (1976).

[39] J.L. Chaboche, Eur. J. Mech. A/Solid **13**, 501-518 (1994).

[40] N. Ohno, J.D. Wang, Int. J. Plasticity **9**, 375-389 (1993).

[41] Y. Jiang, P. Kurath, Int. J. Plast. **12**, 387-415 (1996).

[42] F. Dunne, N. Petrinic, Introduction to Computational Plasticity, Oxford University Press, New York (2005).

[43] M. Aleyaasin, Mechanics of Finite Deformation and Fracture, Apple Academic Press, Oakville (2016).

[44] K. Chung, T. Park, Int. J. Plast. **45**, 61-84 (2013).

[45] P. Thamburaja, B. Klusemann, S. Adibi, S. Bargmann, App. Phys. Lett. **106**, 1-4 (2015).

[46] B. Möller, M. Beer, Fuzzy Randomness, Springer-Verlag, Berlin Heildelberg (2004).

[47] B. Möller, W. Graf, M. Beer, Comput Mech. **26**, 547-565 (2000).

[48] A. Skrzat, M. Wójcik, ZN Politechniki Rzeszowskiej. Mechanika **90** (4), 505-518 (2018).

[49] A. Skrzat, Arch. Metall. Mater. **56**, 559-568 (2011).

[50] A. Skrzat, Wybrane problem eksperymentalnego i numerycznego wyznaczania naprężeń własnych w kołach pojazdów szynowych, Oficyna Wydawnicza Politechniki Rzeszowskiej, Rzeszów (2012).